RSC Advances

PAPER

View Article Online
View Journal | View Issue

Cite this: *RSC Adv.*, 2017, **7**, 18178

Synthesis of phthalate-free plasticizers by hydrogenation in water using RhNi bimetallic catalyst on aluminated SBA-15†

Duc-Ha Phan-Vu and Chung-Sung Tan *

In this study, rhodium–nickel bimetallic nanoparticles loaded on aluminated silica (RhNi/Al-SBA-15) were used as catalysts for the hydrogenation of phthalate in water to produce environmentally acceptable non-phthalate plasticizers. Chemical fluid deposition (CFD) was used to dope metals onto the aluminated silica support, which helped to create a uniform structure of RhNi on Al-SBA-15. The introduction of Ni helped to reduce the use of expensive Rh and increase the number of metal active sites by reducing the bimetallic nanoparticle size. Aluminated SBA-15 not only acted as the support for the RhNi bimetallic catalyst but also enhanced the reaction efficiency by introducing Brønsted and Lewis acid sites and the absorption of phthalates on the catalyst in water. The physicochemical properties of prepared catalysts were characterized by N_2 adsorption–desorption isotherm, X-ray diffraction (XRD), *in situ* diffuse reflectance infrared Fourier transform spectroscopy (DRIFTS), Scanning electron microscopy (SEM), and Transmission electron microscopy (TEM). The catalytic performance of the synthesized catalysts was evaluated with the hydrogenation of dimethyl phthalate (DMP). Despite the low solubility of DMP in water, the hydrogenation using $Rh_{0.5}Ni_{1.5}$/Al-SBA-15 was carried out with an 84.4% reaction yield (*cis*- : *trans*- = 97.5 : 2.5) at 80 °C using 1000 psi of H_2 after 2 h.

Received 22nd February 2017
Accepted 20th March 2017

DOI: 10.1039/c7ra02227a

rsc.li/rsc-advances

Introduction

Phthalate plasticizers have been widely used in the plastic industry to enhance the flexibility and durability of plastic products, especially for polyvinyl chloride (PVC). The total global market for plasticizers has grown up from 5.6 million metric tons in 2008 (ref. 1) to 8.4 million metric tons in 2014.[2] Moreover, it is estimated to reach a market value of US $19.4 billion by 2019. The growth rate is forecasted to expand approximately 6.35% annually,[3] with 87% of this growth being phthalate plasticizers. In most PVC derivative products, the phthalate content is up to 40% of the total weight. However, phthalates are found to be one of the main chemical agents causing cancer, obesity and reproductive problems by disrupting the endocrine system, as shown in recent reports.[4–8] Humans can be exposed to phthalates through PVC medical devices,[9] food packaging,[10–12] children's toys,[13–15] *etc.* In the human body, phthalates interact with human ketosteroids, such as androgen, progesterone, and glucorticoid,[16] thus potentially causing antisteroidal activity. Additionally, phthalates such as di-isododecyl phthalate and di-*n*-octyl phthalate can bind with proteins and affect the conformation and function of the human serum albumin.[17] Thus, this phenomenon results in a potential risk to human health.

Cyclohexane dicarboxylic acid (CHDA) ester plasticizers (or phthalate-free plasticizers) are mainly synthesized by hydrogenating the benzyl ring of phthalates and have gained the interest of scientists due to their advanced physical properties and low toxicity.[18–20] Phthalates possess a benzyl ring structure connected with two moderately electron-withdrawing groups – carboxyl groups. Therefore, it is difficult for hydrogen to attack the aromatic ring and hydrogenate the benzyl ring. Consequently, conventional phthalate hydrogenation requires noble metal catalysts[21–23] or catalysts with a high metal loading[24] and consumes a large amount of organic solvents under harsh conditions to accelerate the reaction. Therefore, Ni was used in this study to reduce the amount of Rh in the catalyst. Rhodium acts as the primary catalyzing agent to break the conjugated bond in the benzyl ring, and nickel plays a role in further hydrogenating the intermediates to the saturated cyclohexane ring. The phthalate molecules travel along the channels of the aluminated SBA-15 and interact with the metal active sites to form the cyclohexane ring products. Therefore, the formation of side products is limited. Additionally, water was used as an effective solvent for the hydrogenation of phthalates due to its environmentally friendly properties.

Aluminated supports have been reported to enhance the efficiency of hydrogenation.[25–28] The presence of Al sites in

Department of Chemical Engineering, National Tsing Hua University, Hsinchu 30013, Taiwan, ROC. E-mail: cstan@mx.nthu.edu.tw; Fax: +886 3572-1684; Tel: +886 3572-1189

† Electronic supplementary information (ESI) available. See DOI: 10.1039/c7ra02227a

porous support structures plays three major roles: (1) helping to increase the uptake of metal complexes onto the support in the metal loading step using chemical fluid deposition (CFD);[29,30] (2) strengthening the interactions of metal species with the support as an anchoring site;[31] (3) enhancing the reaction efficiency with Lewis and Brønsted acid sites.[24] Moreover, due to the acidic properties possessed by the aluminated support, the basic phthalates can be more readily adsorbed by the aluminated support, which is beneficial for the subsequent hydrogenation.

Compared to conventional methods, such as wet impregnation (WI), CFD possesses some advantages[32] due to the unique characteristics of supercritical CO_2, including tunable solvent power through the operational conditions, lack of retention on the substrates after treatment, low surface tension, low viscosity. Therefore, CFD was used to successfully load the metal onto the porous supports.[32] It has shown its superiority to the other loading methods, such as WI, incipient wetness impregnation and co-precipitation. The extremely low surface tension of supercritical CO_2 helps carry organometallic precursors to deep support channels and uniformly load them onto the supports, leading to an increase in the number of metal active sites. After the incorporation of the substrate with the precursor, the organometallic precursor can then be converted to its metal form by the following means:[33] (1) chemically reducing the metal complexes in the supercritical fluid (SCF) using a reducing agent, such as hydrogen or alcohols; (2) thermally reducing the metal complexes in the SCF; (3) thermally decomposing the metal complexes in an inert gas environment, or chemically converting them using hydrogen or air after depressurizing the SCF out of the reactor. Several heterogeneous catalysts were successfully synthesized by CFD using $scCO_2$ as a solvent. Yu *et al.*[34] prepared RhPt/SBA-15 by CFD and demonstrated that RhPt/SBA-15 is superior to both Rh/SBA-15 and Pt/SBA-15. The superior behavior might be due to the cooperating effects of Pt and Rh, with Pt enhancing the adsorption of the starting materials on the active sites and Rh acting as the activated catalytic sites for hydrogenation. Yen *et al.*[35] carried out the hydrogenation of bisphenol A in water using the Ru/MCM-41 catalyst prepared by CFD, and a high reaction efficiency was achieved with this catalyst, while the low solubility of reactants was not an obstacle for the hydrogenation. Ru, Rh, and Pd monometallic nanoparticles and Ru–Rh, Ru–Pd, and Rh–Pd bimetallic nanoparticles on MCM-41 were prepared by Yen *et al.*[36] using CFD. Ru/MCM-41 was prepared by CFD and possessed the highest catalytic activity for the hydrogenation of *p*-xylene, which was nearly 8 times higher than Ru/MCM-41 prepared by conventional methods. The catalytic activity of Rh–Pd/MCM-41 was higher than the activity of individual monometallic catalysts.

Experimental

Materials

Rhodium(III) acetylacetonate ($Rh(acac)_3$, 97%) and nickel(II) acetylacetonate ($Ni(acac)_2$, 95%) were purchased from Stream Chemicals Inc. CO_2 and H_2 gases with purities >99.9% were purchased from Boclh Industrial Gases Co. (Taiwan). *o*-Phthalic acid (PA, 99%), tetrahydrofuran (THF, 99.9%) and dimethyl sulfoxide-d_6 (DMSO-d_6, 99.9 atom% D) were purchased from Sigma-Aldrich. Dimethyl phthalate 99%, *m*-phthalic acid (IPA, 99.9%), and *p*-phthalic acid (TPA, 99%) were purchased from Alfa Aesar. All chemicals were used without any further purification unless noted.

Catalyst preparation

The hexagonal mesoporous silicas SBA-15 and Al-SBA-15 were synthesized following the procedure of Klimova *et al.*[31]

The porous silica SBA-15 was synthesized using poly (ethylene oxide)-*block*-poly(propylene oxide)-*block*-poly(ethylene oxide) triblock copolymer Pluronic P123 as the structure directing agent and tetraethyl orthosilicate (TEOS) as the silica source. First, 4 g of Pluronic P123 was dissolved in 26 g of water and then stirred for 1–2 h at 40 °C to ensure the P123 completely dissolved. Then, 116 g of 2 M HCl solution was used as a pH modifying agent for the P123 solution. After stirring the acidic mixture for 2 h at 40 °C, 8.50 g of TEOS was added into the solution at the rate of 0.05 mL s^{-1} under stirring conditions. The mixture was continuously stirred at 40 °C for 20 h and then aged at 80 °C for 24 h without stirring. The solid product was collected by filtration and washed with deionized water until the washed liquor reached the neutral pH. Then, the solid was calcined at 540 °C for 6 h in static air, and the final product was SBA-15.

Aluminum(III) chloride, $AlCl_3$, was used as the aluminum source in this study. In a typical trial, 1 g SBA-15 with 0.247 g anhydrous $AlCl_3$ were dispersed in 100 mL of dry ethanol. After stirring at 40 °C for 6 h, the aluminum doped solid was separated by filtration. Then, 200 mL of dry ethanol was used to wash the Cl^- ions out of the Al-SBA-15. The solid was dried at 65 °C for 2 h before calcination at 550 °C under static air for 6 h. The final solid Al_5-SBA-15 was then used as the support for the immobilization of Rh and Ni nanoparticles.

Rhodium(III) acetylacetonate, $Rh(acac)_3$, and nickel(II) acetylacetonate, $Ni(acac)_2$, were used as the CO_2 soluble Rh and Ni metal precursors in this study, respectively. CFD was used to load metals onto the supports. From the study of Yu *et al.*,[34] the solubilities of the metal acetylacetonates are relatively lower in $scCO_2$ compared to in THF. Therefore, to achieve the desired theoretical metal loading of Rh and Ni, the required amounts of $Rh(acac)_3$ and $Ni(acac)_2$ were first dissolved in 15 mL tetrahydrofuran (THF). The liquid mixture precursor was added to the solid supports and ultra-sonicated for 2 h to homogenize the precursor and accelerate its diffusion rate into the support channels. THF was then removed by rotary vacuum evaporation. The solid mixture was transferred to a high pressure stainless steel autoclave which was filled with 2500 psi of CO_2 at 50 °C. The mixture in the autoclave was stirred at 50 °C for 3 h before depressurization. After depressurization, the solid is the as-synthesized catalyst with organometallic precursors in the support channels. The organometallic precursors were converted into elemental metal by calcining the as-synthesized catalyst at 400 °C under an air flow for 4 h followed by

reduction under a hydrogen flow at 400 °C for 4 h. After reduction, pure nitrogen was used to remove the excess hydrogen inside the calcination furnace before collecting the final catalyst.

Catalyst characterization

N_2 adsorption–desorption experiments were performed using a physical adsorption instrument (Quantachrome Autosorb-1-MP). The specific surface area was measured using BET method, pore volume and pore size were calculated by BJH method. The conformation and structure of the catalyst were characterized *via* (1) X-ray diffraction analysis (Ultima IV Multipurpose X-ray diffraction system) using Cu Kα radiation source at 40 kV and 20 mA and a scan rate of 1° min^{-1} in the 2θ range from 30 to 90°; and (2) low-angle X-ray diffraction (Bruker D8 advance X-ray diffraction system) using Cu Kα with an acceleration voltage of 40 kV and a filament current of 40 mA, the scanning angle varied between $0.5^\circ \leq 2\theta \leq 5^\circ$. The scanning electron microscopy (SEM) analysis was performed on a UHR Cold-Emission FE-SEM SU8000 Series SEM machine. The samples were dried and doped on carbon tape followed by vacuum activation before analysis. Transmission electron microscopy (TEM) analysis was performed using a JOEL JEM-2100 transmission electron microscopy. A small quantity of the sample that was dispersed in ethanol followed by ultrasonication for 5 minutes; then, carefully placed on a carbon coated copper grid (200 mesh) and the grid was dried overnight under vacuum.

The experimental setup of the *in situ* FTIR study of pyridine adsorption on various supports and catalysts is shown in Fig. S1.† The setup consists of (1) a gas flow controller; (2) an FTIR bench (Thermo Nicolet 6700 FTIR spectrometer with an MCT/B detector) equipped with a diffuse reflectance infrared Fourier transform spectroscopy (DRIFT) reactor (Harrick Scientific); (3) a pyridine saturator and (4) a homemade automated temperature controller with a LabView DAQ module. The spectra were collected at a resolution of 4.0 cm^{-1} with 32 co-added scans for each spectrum.

To examine the acidic sites on the supports and the catalyst surface, *in situ* pyridine adsorption experiments were carried out, similar to the previous works of Stevens *et al.*[37,38] 50 mg of the sample was used in each test and was loaded into the DRIFT reactor. Samples were first heated *in situ* from RT to 873 K at a rate of 10 K min^{-1} and held for 120 min under an 80 sccm argon flow. This pretreatment process was employed to remove surface organics and water adsorbates to create a clean condition.

After pretreatment, the sample and reactor were cooled down to 413 K for the pyridine adsorption experiment. This temperature was chosen to prevent pyridine (b_p = 389 K) condensation on the sample surface. Gaseous pyridine was flowed into the reactor by re-directing Argon through the pyridine saturator. Each sample was exposed to an Ar/pyridine mixture gas for 30 min to ensure saturated adsorption. Then, at 413 K, the gas was switched to pure Ar to remove all excessive pyridine, including the weakly adsorbed (physisorbed) pyridine on the sample surface until no change was observed in the FTIR spectra. Finally, in an Ar atmosphere, the sample and reactor were cooled down to RT. All the above processes were monitored and recorded by FTIR.

Hydrogenation of dimethyl phthalate (DMP) and phthalic acids

RhNi bimetallic catalysts on aluminated supports were used for DMP hydrogenation to evaluate the catalytic performance. The hydrogenations were carried out in a 200 mL high-pressure stainless steel autoclave. All pressure and temperature parameters, controllers, and heaters were installed properly.

In a typical experiment, 1.0 g of DMP, 50.0 mg of the catalyst and 50 mL of D.I. water were added to a closed high-pressure autoclave. The reactor was then purged three times with hydrogen to remove the remaining air inside the reactor. After the autoclave was brought to the desired temperature, 1000 psi of hydrogen was fed to start the reaction. The reaction was carried out for 1–4 h with a constant stirring rate of 500 rpm. After the hydrogenation, the products were extracted with diethyl ether with 0.2 g of benzyl benzoate as the external standard in a GC-MS for further analysis. The hydrogenations of phthalic acids were carried out under similar conditions, and the reaction yields were determined by ^{1}H-NMR (500 MHz, DMSO, Varian Unity Inova, 500 NMR). After the reaction system was cooled down to room temperature and depressurized, water was removed from the reaction mixture by evaporation. Then the crystals including phthalic acid and the corresponding products were collected and dried overnight. Dimethyl sulfoxide-d_6 was used as a diluting solvent to prepare samples for NMR analysis.

Results and discussion

Conformation and structure of RhNi/Al-SBA-15 catalysts

A series of Rh and Ni monometallic catalysts and RhNi bimetallic catalysts using SBA-15 and Al_5-SBA-15 supports were prepared by CFD using $scCO_2$ as the solvent in this study. The catalysts were denoted based on the weight ratio between the metals and the support as Rh_xNi_y/Al_z-SBA-15 where x represents the ratio of Rh : Al_5-SBA-15, y represents the ratio of Ni : Al_5-SBA-15, and z represents the ratio of Al : SiO_2.

Fig. 1 shows the small-angle XRD patterns of SBA-15, Al_5-SBA-15 and $Rh_{0.5}Ni_{1.5}/Al_5$-SBA-15. The small-angle XRD patterns of the catalysts and supports are similar with an intense main peak (100) and two main peaks (110) and (200) plane reflections. The largest peak (100) gives a d_{100} spacing (106–114 Å), which is analogous to the large lattice parameter (a_o = 122–132 Å) of SBA-15.[39] The diffraction patterns also confirm the invariance of the SBA-15 structure after alumination with $AlCl_3$ and the successful loading of Rh and Ni by CFD.

The X-ray diffraction patterns of Rh and Ni monometallic catalysts and a series of RhNi bimetallic catalyst with different metal ratios are shown in Fig. 2. The specific peaks of the Rh and Ni monometallic catalysts are clearly observable, indicating that the reduction with hydrogen successfully turned the metal precursors into elemental metals. The XRD pattern for Rh_2/Al_5-

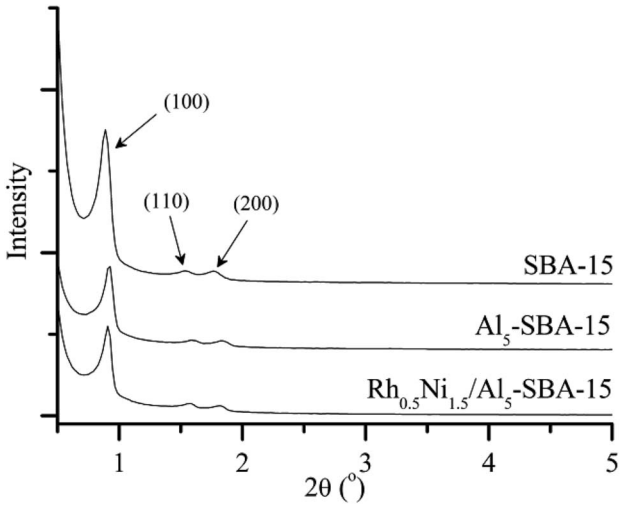

Fig. 1 Small-angle X-ray diffraction patterns.

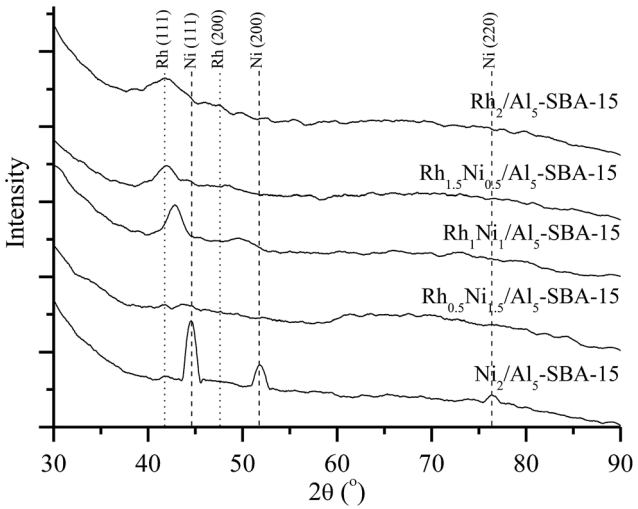

Fig. 2 XRD diffractogram of Rh and Ni monometallic catalysts and RhNi bimetallic catalysts.

SBA-15 shows two diffraction peaks at $2\theta = 41.3°$ and 47.7°, which represent the (111) and (200) planes of the face-centered cubic (fcc) structure Rh (JCPDS 5-685), respectively. The representative XRD diffraction peaks of the Ni_2/Al_5-SBA-15 located at $2\theta = 44.3°$, 51.7°, and 76.2° can be, respectively, indexed to the (111), (200), and (220) planes of the metallic phases of Ni (JCPDS 4-850) formed by the reduction of the Ni precursor. Due to the similar structure of Rh and Ni particles, the prepared RhNi bimetallic nanoparticles were present as alloy with a fcc structure.

In the XRD patterns of the RhNi bimetallic catalysts on Al_5-SBA-15, the introduction of a small amount of Rh slowed and broadened the specific peak of catalyst in the XRD pattern.[40] Additionally, the peaks tend to shift to the left, probably due to the formation of a RhNi alloy.

The SEM images of the supports in Fig. 3 indicate that the cylindrical shape of SBA-15 remained unchanged after being modified with Al. The size of the support was approximately 1

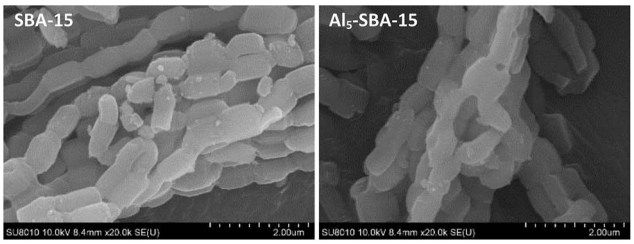

Fig. 3 SEM images of the supports.

μm in length and 0.5 μm in diameter. The SBA-15 particles were relatively uniform in size and shape confirming the reliability of the preparation method. Furthermore, the SBA-15 particles stuck to each other along the (001) faces, forming long rods of adhered particles. This phenomenon is commonly observed for SBA-15 materials.[41]

TEM images of the calcined catalysts are shown in Fig. 4. The TEM images of the monometallic catalysts show that the smaller sized Rh dispersed in the support while the larger Ni particles located in the siliceous support due to the low solubility of $Ni(acac)_2$ in $scCO_2$.[42] This phenomenon is consistent with existing observations.[43] Among the RhNi bimetallic catalysts, $Rh_{0.5}Ni_{1.5}/Al_5$-SBA-15 possessed the smallest metal particle size regardless of the high loading of the Ni precursor. The possible reason is that the introduction of Ni helped reduce the particle size of the primary metal.

Fig. 5a presents the pore size distribution of the Rh monometallic catalyst prepared by CFD and WI using SBA-15 and Al_5-SBA-15 supports. In the pore size distribution pattern, the highest peak of the catalysts prepared using the SBA-15 support appeared at 6.6 nm for CFD and 6.3 nm for WI. However, for the catalysts prepared using Al_5-SBA-15, the main peak was at 4.9 nm for CFD and 5.6 nm for WI. In Fig. S3,† the elemental mapping of Al_5-SBA-15 using SEM analysis confirmed the presence of Al sites on the outer surface of the support. The reason for this difference therefore might due to the adsorption effects of the support containing Al, which could attract more metal acetylacetonate precursors onto the acidic surface. Therefore, the pores contained more metal nanoparticles after

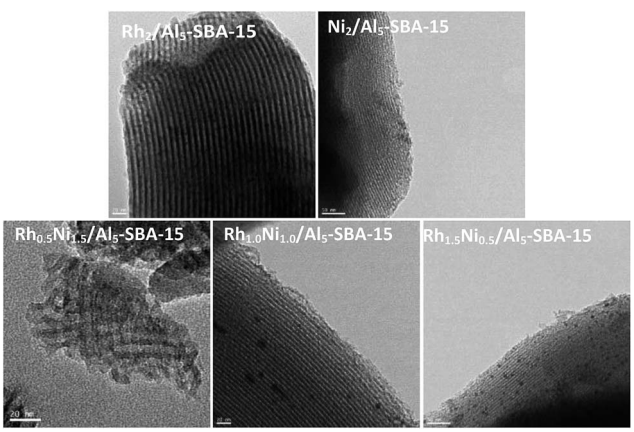

Fig. 4 TEM images of Rh, Ni monometallic catalysts and RhNi bimetallic catalysts.

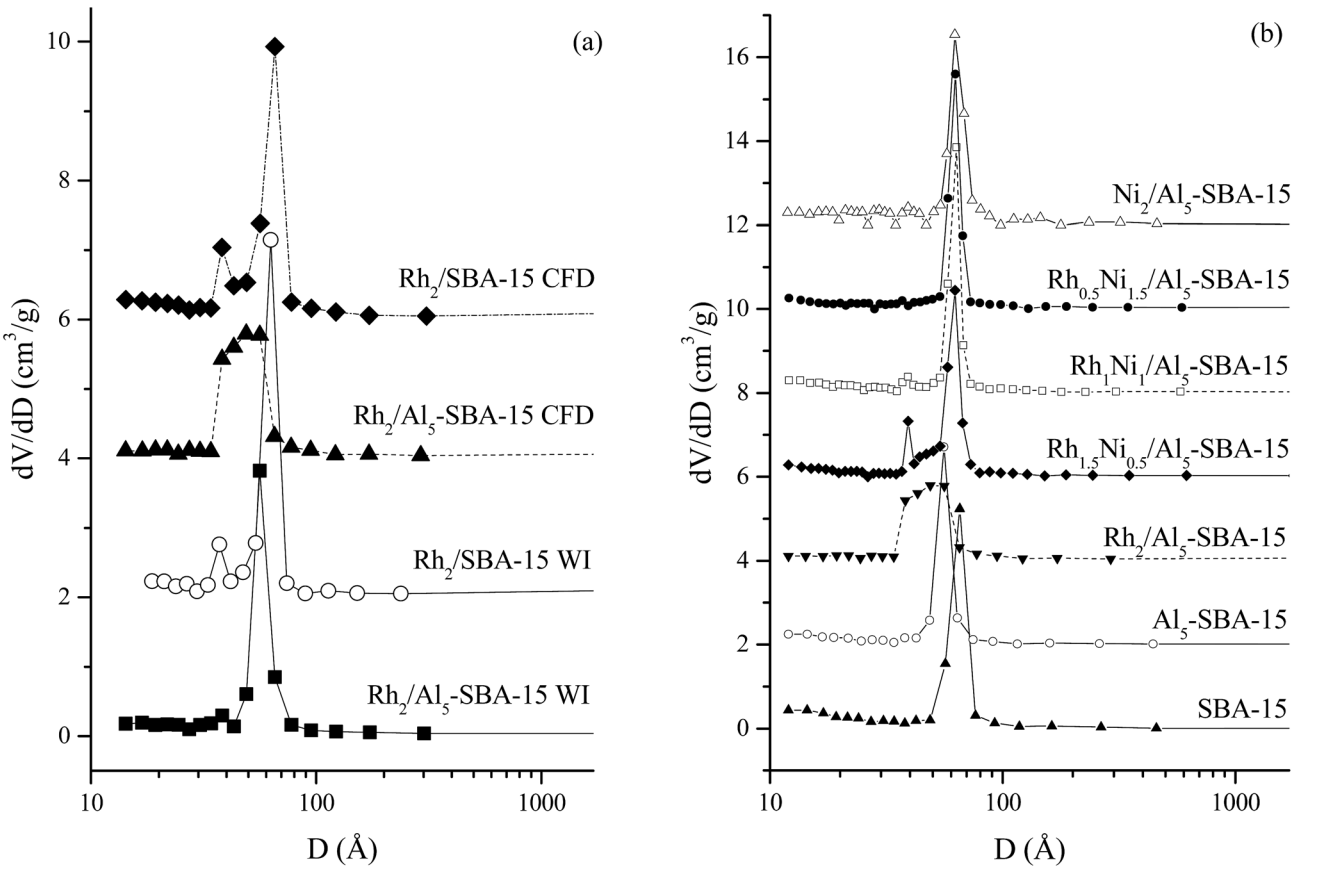

Fig. 5 Pore size distribution of the Rh catalyst on SBA-15, Al_5-SBA-15 (a) and the RhNi catalysts on Al_5-SBA-15 (b).

loading, causing the decrease in the pore size. Moreover, the Rh in SBA-15 and Al_5-SBA-15 had two main peaks for the pore size distribution pattern. This was probably due to the deposition of the metal precursor at the pore entrance. In contrast, the Rh_2/Al_5-SBA-15 synthesized using CFD possessed a broad peak that overlapped the two main peaks, which proves the increased loading of metal in the pores. Thus, for Al_5-SBA-15 support, the elemental mapping was consistent with the pore size distribution. On the other hand, perhaps the catalyst synthesized by CFD using the Al-SBA-15 support could possess a more uniform structure of metal nanoparticle than the untreated SBA-15 support.

Fig. 5b shows the pore size distribution of the RhNi bimetallic catalyst with different metal ratios on the Al_5-SBA-15 support using CFD. SBA-15 and Al_5-SBA-15 pore size distribution patterns were used as the comparison standards. Rh_2/Al_5-SBA-15 possessed a broad peak from 3.9 nm to 6.4 nm. $Rh_{1.5}Ni_{0.5}/Al_5$-SBA-15 and Rh_1Ni_1/Al_5-SBA-15 possessed two separated peaks at 3.9 nm and 6.3 nm, respectively, and the $Rh_{0.5}Ni_{1.5}/Al_5$-SBA-15 contained only one peak at 6.3 nm which is similar to the main peak of Ni_2/Al_5-SBA-15. Thus, the introduction of Ni into the Rh catalyst helped reduce the size of the bimetallic nanoparticles. Therefore, the nanoparticles could be deposited onto the pore walls instead of the pore entrance as was in the case of Rh_2/Al_5-SBA-15.

Each of the SBA-15, Al_5-SBA-15 and catalysts prepared from the Al_5-SBA-15 support exhibited a type IV isotherm with two sharp reflections at the relative pressure of 0.6–0.8. In addition, the H1 hysteresis loop endorses the natural structure of the SBA-15. The isotherm curves are shown in Fig. S2.†

Enhanced acidic properties of aluminated SBA-15 over untreated SBA-15

The DRIFTS analytical results (Fig. 6) and the calculated Brønsted and Lewis acid site intensities (Table 1) proved the increased acidity from SBA-15, Al_5-SBA-15, and $Rh_{0.5}Ni_{1.5}/Al_5$-SBA-15.

For SBA-15, the Lewis acid site intensity was 0.093 and the Brønsted acid site intensity was 0.043, while, with the small introduction of Al to SBA-15, the Lewis and Brønsted acid site intensities of Al_5-SBA-15 were 0.133 and 0.156, respectively. Thus, Al was proven to be successfully doped on the SBA-15 using the procedure. This result was consistent with the pore size distribution, the enhancement of support acidity leaded to the decrease of pore size due to the presence of Al coated on the channel surface. Moreover, the introduction of Al helped boost the acidity of the material, which is necessary for hydrogenation. The introduction of Al and RhNi bimetallic nanoparticles also enhanced the peak of the hydroxyl group.

In the study of Hensen *et al.*,[44] Al-SBA-15 supports which were synthesized under acidic conditions have lower Brønsted acidity than desired. The reason is though a sustaintial part of Al is in tetrahedral coordination, but the acidity was mainly

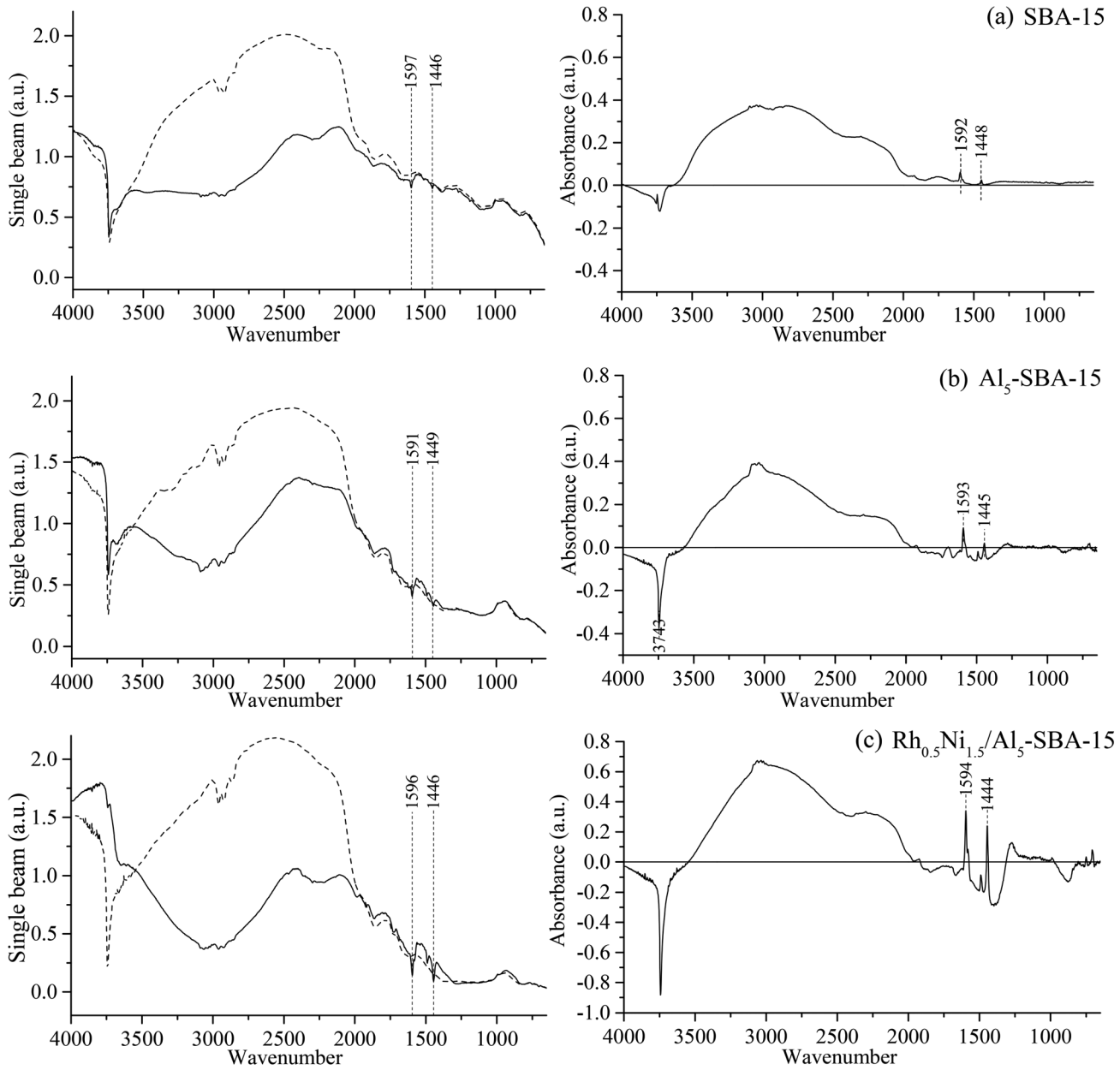

Fig. 6 Single beam (left) and absorbance (right, using spectrum before pyridine adsorption as the background) spectra of the samples before (dash line) and after (solid line) pyridine adsorption for (a) SBA-15; (b) Al_5-SBA-15; (c) $Rh_{0.5}Ni_{1.5}/Al_5$-SBA-15.

Table 1 Brønsted and Lewis acid site intensities

Sample	SBA-15	Al_5-SBA-15	$Rh_{0.5}Ni_{1.5}/Al_5$-SBA-15
Raw Lewis acid site intensity (1445 cm^{-1})	0.035	0.052	0.310
Raw Brønsted acid site intensity (1600 cm^{-1})	0.016	0.061	0.269
Normalized factor	0.375	0.391	0.682
Normalized Lewis acid site intensity (1445 cm^{-1})	0.093	0.133	0.445
Normalized Brønsted acid site intensity (1600 cm^{-1})	0.043	0.156	0.394

contributed by Al on the surface, not Al in the network. Therefore, in our research, the Brønsted acidity was enhanced because Al coated on SBA-15 surface as a layer and maximize the efficiency of Al sites. This Al layer can strengthen the bond between RhNi nanoparticles and support surface, also provide acid sites for hydrogenation.

Catalytic performance of RhNi/Al-SBA-15 bimetallic catalysts tested on DMP hydrogenation

The catalytic activities of the Rh/Al_5-SBA-15 catalysts prepared by CFD and WI for the hydrogenation of dimethyl phthalate (DMP) were tested in water at a temperature range varying from 30 to 80 °C with an H_2 pressure of 1000 psi for 1 h. The experimental results (Fig. 7a) showed that the catalysts prepared by the CFD method exhibited much better performance than those prepared by the WI method. At 60 °C, an 87.5% yield towards dimethyl 1,2-cyclohexanedicarboxylate (DMCHDA) was achieved by the catalysts prepared by CFD, while only a 67.1% yield was obtained by the catalyst prepared with the WI method. The reason for the improved performance of the CFD-prepared catalyst was due to the presence of more metal active sites. By applying the CFD method, the metal precursors could be uniformly dispersed onto the support surface, therefore the active metal sites were increased.

To demonstrate the effects of the aluminated support, Al_5-SBA-15 and SBA-15 were used as siliceous porous supports for the preparation of the Rh monometallic catalysts. The catalyst performance results in Fig. 7a show a significant improvement for using the aluminated support. At 30 °C, a 44.9% yield towards the DMCHDA was generated using the Rh catalyst with the aluminated support, however, the selectivity was only 11.5% using a non-aluminated support. The aluminated mesoporous silica (Al-SBA-15) helps increase the catalyst performance by increasing the metal precursor uptake, strengthening the bond between the metal and the support, and providing acid sites which are necessary for hydrogenation.

To determine the optimal metal ratio of Rh to Ni, DMP hydrogenation was carried out using various metal ratios. The results in Fig. 7b show that the catalyst with a Rh : Ni ratio of 0.5 : 1.5 ($Rh_{0.5}Ni_{1.5}$/Al_5-SBA-15) exhibited the best performance among the tested bimetallic catalysts, a reaction yield of 61.9% at 80 °C was observed, while a yield of only 28.6% was shown using the catalyst Ni_2/Al_5-SBA-15. $Rh_{1.5}Ni_{0.5}$/Al_5-SBA-15 had a slightly higher catalytic performance compared with Rh_1Ni_1/Al_5-SBA-15 due to the higher content of Rh. The enhanced catalytic performance of $Rh_{0.5}Ni_{1.5}$/Al_5-SBA-15 might be due to the higher catalytic sites from the formation of smaller particles when a suitable amount of Ni was introduced into the catalyst.

To examine if the catalyst performance could be increased at high contents of Ni in the RhNi bimetallic catalysts, Rh was

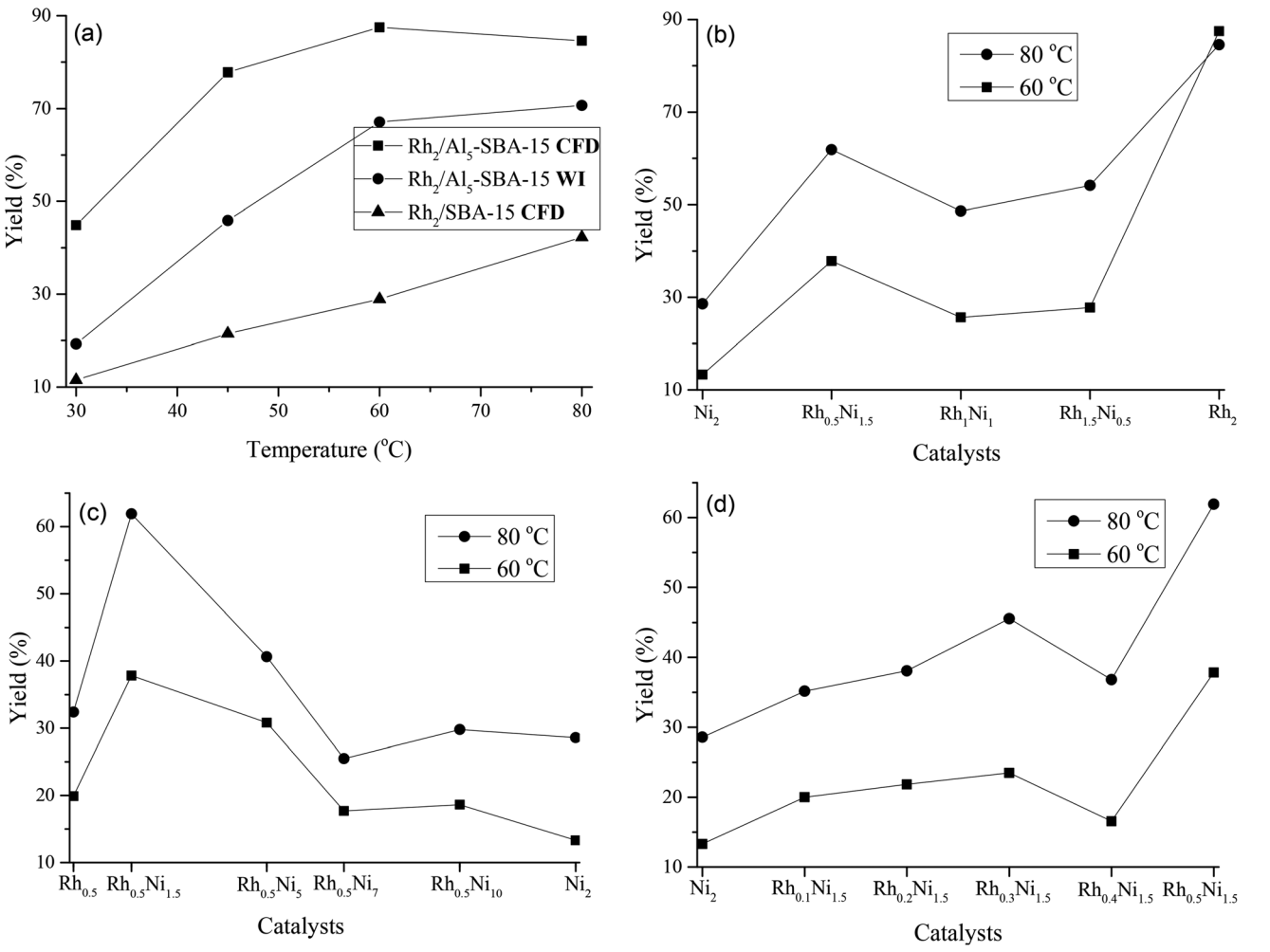

Fig. 7 Experimental results for the catalyst optimization. (a) Effects of the preparation methods and support properties; (b) effects of the Rh : Ni metal ratio with a total loading of 2 wt%; (c) effects of high Ni loading; and (d) effects of low Rh loading.

fixed at 0.5 wt% while the Ni content was varied from 1.5, 5, 7, and 10 wt% for DMP hydrogenation in water at 60 and 80 °C at a H_2 pressure of 1000 psi for 1 h. The results in Fig. 7c demonstrate that an increase of the Ni content led to a decrease of the catalyst performance, due to the Rh metal active sites being occupied by more Ni nanoparticles.

The concentration of Rh in the RhNi bimetallic catalyst was varied from 0.1 wt% to 0.5 wt%, and the concentration of Ni was kept constant at 1.5 wt%. The RhNi bimetallic catalysts with a 0.1–0.5 wt% of Rh were used for DMP hydrogenation at 60 °C and 80 °C and 1000 psi of H_2 for 1 h. From the experimental results, Fig. 7d shows that a decrease in the amount of Rh loaded onto SBA-15 led to a decrease in the performance of the catalytic hydrogenation of DMP. This was because the Rh acted as a facilitating agent in the initiation step. When the Rh amount decreased, the first step of benzyl ring hydrogenation became slower, which, consequently, caused a decrease in the catalytic performance. The drop in the catalytic performance of $Rh_{0.4}Ni_{1.5}$-Al_5-SBA-15 was probably due to the formation of bigger nanoparticles, therefore, the number of catalytic sites decreased.

Therefore, RhNi/Al-SBA-15 had the best catalytic performance at Rh : Ni ratio of 0.5 wt% : 1.5 wt% using Al_5-SBA-15 as support. The reason is due to the RhNi nanoparticles size and acidity of Al_5-SBA-15. $Rh_{0.5}Ni_{1.5}/Al_5$SBA-15 possessed the smallest nanoparticle size among other RhNi bimetallic nanoparticles. Thus, the amount of metal active sites is increased. Moreover, the presence of Al layer on SBA-15 surface help strengthening bonds between RhNi nanoparticles and support, thus reduce the leaking of metal out of catalyst's structure during reaction. On the other hand, the presence of Al contributed to the reaction efficiency due to the introduction of Brønsted and Lewis acid sites.

Effects of process conditions on catalytic performance

$Rh_{0.5}Ni_{1.5}/Al_5$-SBA-15 was used as the catalyst to examine the effects of H_2 pressure on the DMP hydrogenation. The reactions were carried out at 80 °C for 1 h with different H_2 pressures. As seen from the experimental results (Fig. 8), the reaction efficiency was higher when the H_2 pressure increased since the higher H_2 pressure led to a higher solubility of H_2 into water.

Additionally, Fig. 8 shows that the reaction yield increased with the increasing reaction time. When a H_2 pressure of 1000 psi was chosen, the reactions were carried out at 80 °C with reaction times of 1, 2, and 4 h. Rh_2/Al_5-SBA-15 completely hydrogenated DMP to DMCHDA after 2 h, compared to an 84.4% reaction yield when $Rh_{0.5}Ni_{1.5}/Al_5$-SBA-15 was used. When $Rh_{0.5}Ni_{1.5}/Al_5$-SBA-15 was used, a 95.8% reaction yield was achieved after reacting for 4 h. Therefore, the reaction time was fixed at 2 h for further experiments.

Reaction mechanisms

To understand why 97.5% of the products were *cis*-isomers using $Rh_{0.5}Ni_{0.5}/Al_5$-SBA-15 as the catalyst for DMP hydrogenation in water (1000 psi of H_2 at 80 °C for 2 h), this hydrogenation system was used in different solvents under the same operating conditions. The results of experiments using water, hexane and $scCO_2$ introduced hexane are shown in Table 2.

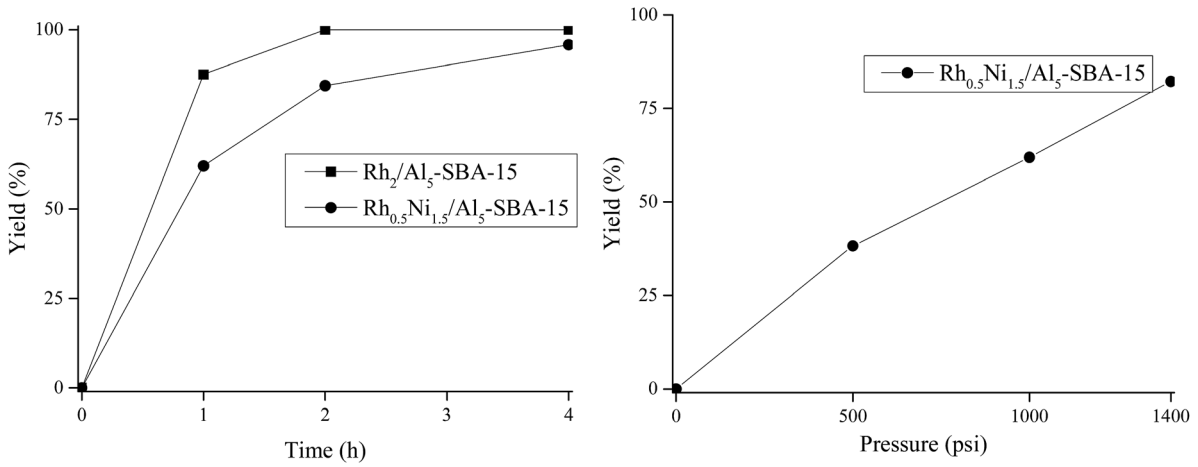

Fig. 8 Experimental results for process condition optimization.

Table 2 Reaction yield and isomer selectivity in different solvents

Solvent	Temp. (°C)	Yield (%)	-*trans* isomer selectivity (%)	-*cis* isomer selectivity (%)
Water	80	84.4	2.5	97.5
Hexane	80	41.9	12.6	87.4
Hexane + $scCO_2$	80	28.5	18.3	81.7
Hexane + $scCO_2$	140	37.9	39.0	61.0

When the solvent was changed from water to hexane and $scCO_2$ introduced hexane, the reaction yield decreased and the *trans*-isomer selectivity increased. The DMP completely dissolved in hexane but not in water. For the DMP hydrogenation using water, acid sites contributed by Al helped to attract DMP molecules onto SBA-15 surface because DMP is slightly basic. Thus, DMP bonded with SBA-15 firmly. H_2 came into SBA-15 pores could attack only one side of DMP to produce mostly *cis*-isomer products. However, when hexane was used, the mobility of the DMP in the catalyst pores was higher. Therefore, the H_2 could interact with both two side of DMP molecules in the presence of catalytic sites to form more *trans*-isomer products. The introduction of $scCO_2$ helped decrease the mixture viscosity, which possibly enhances the mobility of the reactants, DMP and H_2. H_2 could access both sides of the benzyl ring to form more *trans*-isomer products. At 140 °C using hexane and $scCO_2$, both the reaction yield and percentage of *trans*-isomer products increased due to the higher catalyst reactivity and higher diffusion rate of the reactants. The comparison of the reaction efficiency between hexane and $scCO_2$ introduced hexane at different temperatures is shown in Fig. 9.

The reaction yield in the solvent hexane increased with temperature. When $scCO_2$ was introduced into the reaction system, the reaction yield changed insignificantly with the variation of temperature. It was expected in the beginning of the study that the introduction of $scCO_2$ would enhance the reaction efficiency due to a decrease in the solvent viscosity. However, the reaction yield in the case of the introduced $scCO_2$ was found to be lowered. This may be a result of the catalyst poisoning caused by CO_2.[45] The percentage of *trans*-isomer products was higher with increasing reaction temperature, possibly due to the lower viscosity and higher diffusion rate. The reaction mechanism is shown in Fig. 10.

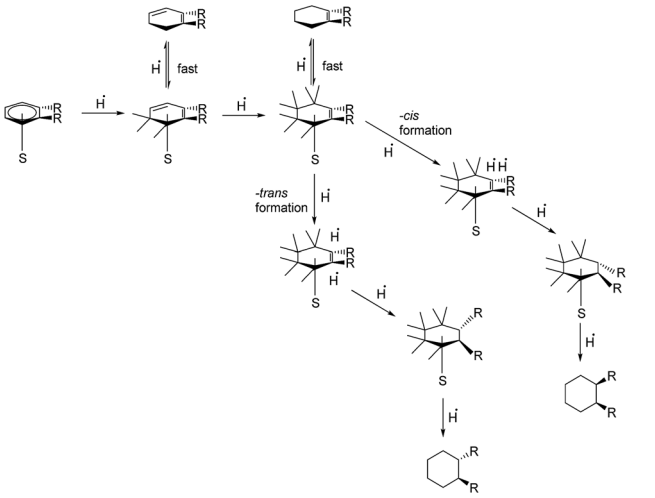

Fig. 10 Proposed reaction mechanisms.

Hydrogenation of phthalic acids

$Rh_{0.5}Ni_{1.5}/Al_5$-SBA-15 was also used as a catalyst for the hydrogenation of phthalic acids in water. ^{1}H-NMR was used to determine reaction yields. The reaction results are shown in Table 3. Among the three phthalic acids, *o*-phthalic acid has the highest solubility in water (0.6 g per 100 mL at 20 °C), *p*-phthalic acid is harder to dissolve in water with a solubility of 0.0015 g per 100 mL at 20 °C, and *m*-phthalic acid is virtually insoluble in water at low temperatures. Therefore, due to the difference in material properties (position of substituent groups, solubility), *o*-phthalic acid is the easiest and *m*-phthalic acid is hardest to hydrogenate with reaction yields of 95.3% and 59.3% after 6 h at 140 °C, respectively.

Table 3 Phthalic acid hydrogenation

Reagent	Solvent	Temp. (°C)	Time (h)	Yield (%)
o-Phthalic acid	Water	80	2	66.6
o-Phthalic acid	Water	140	6	95.3
m-Phthalic acid	Water	140	6	59.3
p-Phthalic acid	Water	140	6	69.8

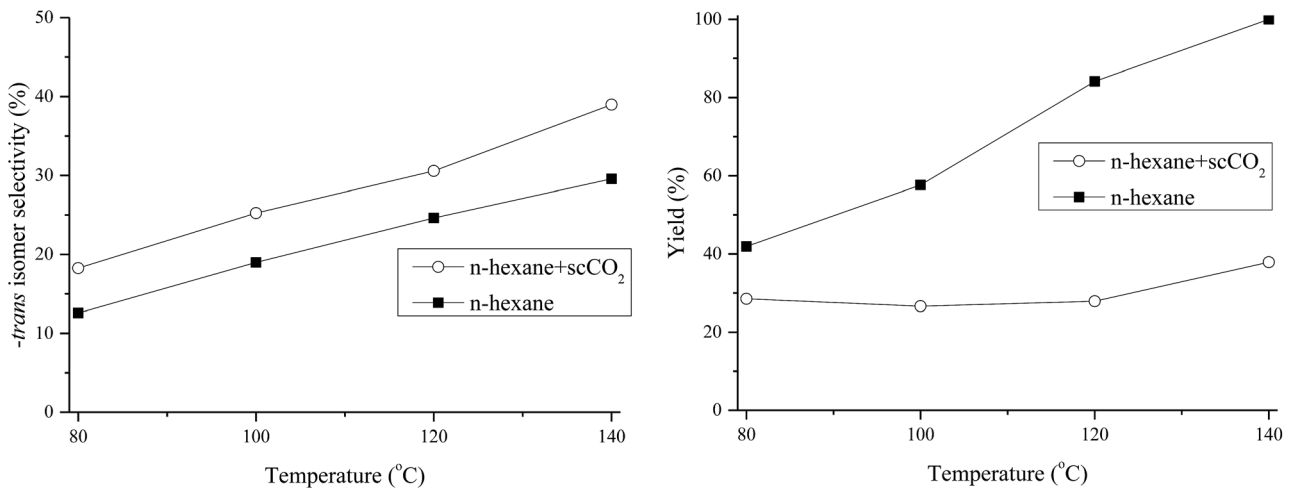

Fig. 9 Comparison of the reaction efficiency between reactions in hexane and hexane + $scCO_2$.

Conclusions

The excellent catalytic properties of Rh were successfully applied for the hydrogenation of DMP. Ni was used as the secondary metal to reduce the amount of Rh used. As a consequence, the optimal metal concentration in the catalyst of Rh and Ni was 0.5 wt% and 1.5 wt%, respectively. The introduction of Al on the catalyst was proven to have positive effects on the reaction efficiency by the enhancement of the material acidity and nanoparticles – support bonds. The elemental mapping visually proved the presence of Al site on the outer surface of the support. The pore size reduction of catalyst was due to the introduction of Al sites and the loading of RhNi nanoparticles, determined by pore size distribution. The DRIFTS analysis confirmed the enhancement of Lewis and Brønsted acid site intensities for the aluminated SBA-15 over conventional SBA-15. On the other hand, the Al layer on the SBA-15 surface also acted as an anchoring site to strengthen the bond of the RhNi bimetallic nanoparticles with the SBA-15 support. The experimental results also confirmed that the introduction of Ni helped to reduce the RhNi nanoparticles size, thus increasing the amount of metal active sites without adding more metal precursors.

Water was used as the solvent for the hydrogenation of the DMP as a green solvent. Though DMP has limited solubility in water, the hydrogenation occurred with high reaction yield. At the optimal operational conditions of 80 °C, 2 h, 1000 psi of H_2, 20 mg $Rh_{0.5}Ni_{1.5}/Al_5$-SBA-15 as the catalyst and 50 mL water as the solvent, 1 g of DMP was hydrogenated with a reaction yield of 84.4%, with most of the product being *cis*-isomers (97.5%). The high selectivity of the *cis*-isomer over the *trans*-isomer is due to the shielding effects of the catalyst in the water environment. Due to the limited solubility of DMP in water and the high absorption to acid sites of catalyst, hydrogen could mostly access one side of the DMP. Therefore, the *cis*-isomer was formed. This phenomenon was confirmed by hexane and $scCO_2$ added hexane. The *trans*-isomer selectivity increased when the solvent viscosity was decreased. This phenomenon can be applicable in medicinal chemistry to synthesize geometric isomers directly from starting materials without requirements of purification step.

The study was also extended to the hydrogenation of *o*-phthalic acid, *m*-phthalic acid and *p*-phthalic acid. The hydrogenation of phthalic acids occurred at 140 °C, 6 h, 1000 psi of H_2, 20 mg $Rh_{0.5}Ni_{1.5}/Al_5$-SBA-15 catalyst and 50 mL water. The *o*-phthalic acid, *p*-phthalic acid and *m*-phthalic acid each have different solubilities in water, 0.6 g per 100 mL, 0.0015 g per 100 mL, and mostly insoluble, respectively. Therefore, *o*-phthalic acid is the easiest and *m*-phthalic acid is the hardest to be hydrogenated with reaction yields of 95.3% and 59.3%, respectively, and the reaction yield for *p*-phthalic acid was 69.8%.

Acknowledgements

The authors like to thank the ROC Ministry of Science and Technology (grant number NN10502-0163) for the financial support.

Notes and references

1 M. D. Bisig, *Plasticizer Update, SPI 20th Vinyl Compounding Conference*, July 19-21, 2009.
2 M. P. Malveda, *Chemical Economics Handbook Report on Plasticizers*, July 2015.
3 *Addit. Polym.*, 2015, **2015**, 10.
4 J. Autian, *Environ. Health Perspect.*, 1973, **4**, 3.
5 D. K. Agarwal, S. Eustis, J. C. Lamb 4th, J. R. Reel and W. M. Kluwe, *Environ. Health Perspect.*, 1986, **65**, 343.
6 F. A. Arcadi, C. Costa, C. Imperatore, A. Marchese, A. Rapisarda, M. Salemi, G. R. Trimarchi and G. Costa, *Food Chem. Toxicol.*, 1998, **36**, 963.
7 P. W. Albro, J. T. Corbett, J. L. Schroeder, S. Jordan and H. B. Matthews, *Environ. Health Perspect.*, 1982, **45**, 19.
8 S. Miles-Richardson, S. Bosch, S. Swarts, F. Llados and D. A. Gray, *Toxicological Profile for Di(2-ethylhexyl)phthalate (DEHP)*, Agency for Toxic Substances & Disease Registry, 2002.
9 J. A. Tickner, T. Schettler, T. Guidotti, M. McCally and M. Rossi, *Am. J. Ind. Med.*, 2001, **39**, 100.
10 J. R. Startin, I. Parker, M. Sharman and J. Gilbert, *J. Chromatogr. A*, 1987, **387**, 509.
11 K. M. Rodgers, R. A. Rudel and A. C. Just, in *Molecular and Integrative Toxicology*, ed. R. R. Dietert, 2014, ch. Phthalates in Food Packaging, Consumer Products, and Indoor Environments, p. 31, DOI: 10.1007/978-1-4471-6500-2_2.
12 A. Fankhauser-Noti, S. Biedermann-Brem and K. Grob, *Eur. Food Res. Technol.*, 2006, **223**, 447.
13 C. F. Wilkinson and J. C. Lamb 4th, *Regul. Toxicol. Pharmacol.*, 1999, **30**, 140.
14 S. Biedermann-Brem, M. Biedermann, S. Pfenninger, M. Bauer, W. Altkofer, K. Rieger, U. Hauri, C. Droz and K. Grob, *Chromatographia*, 2008, **68**, 227.
15 S. I. Korfali, R. Sabra, M. Jurdi and R. I. Taleb, *Arch. Environ. Contam. Toxicol.*, 2013, **65**, 368.
16 M. K. Sarath Josh, S. Pradeep, K. S. Vijayalekshmy Amma, R. Sudha Devi, S. Balachandran, M. N. Sreejith and S. Benjamin, *J. Appl. Toxicol.*, 2016, **36**, 836.
17 Y. Yue, J. Liu, R. Liu, Y. Sun, X. Li and J. Fan, *Food Chem. Toxicol.*, 2014, **71**, 244.
18 A. Schutze, C. Palmke, J. Angerer, T. Weiss, T. Bruning and H. M. Koch, *J. Chromatogr. B: Anal. Technol. Biomed. Life Sci.*, 2012, **895–896**, 123.
19 A. Schütze, M. Kolossa-Gehring, P. Apel, T. Brüning and H. M. Koch, *Int. J. Hyg. Environ. Health*, 2014, **217**, 421.
20 M. J. Silva, T. Jia, E. Samandar, J. L. Preau Jr and A. M. Calafat, *Environ. Res.*, 2013, **126**, 159.
21 X. Li, Z. Sun, J. Chen, Y. Zhu and F. Zhang, *Ind. Eng. Chem. Res.*, 2014, **53**, 619.
22 A. B. Hungria, R. Raja, R. D. Adams, B. Captain, J. M. Thomas, P. A. Midgley, V. Golovko and B. F. Johnson, *Angew. Chem., Int. Ed.*, 2006, **45**, 4782.
23 R. Raja, T. Khimyak, J. M. Thomas, S. Hermans and B. F. G. Johnson, *Angew. Chem., Int. Ed.*, 2001, **40**, 4638.

24 J. Zhao, M. Xue, Y. Huang and J. Shen, *Catal. Commun.*, 2011, **16**, 30.
25 R. X. Yang, K. H. Chuang and M. Y. Wey, *RSC Adv.*, 2016, **6**, 40731.
26 J. R. Restrepo-Garcia, V. G. Baldovino-Medrano and S. A. Giraldo, *Appl. Catal., A*, 2016, **510**, 98.
27 S. Gbadamasi, T. H. Ali, H. V. Lee, A. Y. Atta, P. Sudarsanam, S. K. Bhargava and S. B. A. Hamid, *RSC Adv.*, 2016, **6**, 25992.
28 Y. Wei, Y. Li, Y. Tan, Z. Wu, L. Pan and Y. Liu, *Chem. Eng. J.*, 2016, **298**, 271.
29 G. Micera, L. S. Erre and R. Dallocchio, *Colloids Surf.*, 1987, **28**, 147.
30 J. C. Summers and S. A. Ausen, *J. Catal.*, 1978, **52**, 445.
31 T. Klimova, J. Reyes, O. Gutiérrez and L. Lizama, *Appl. Catal., A*, 2008, **335**, 159.
32 S. E. Bozbağ and C. Erkey, *J. Supercrit. Fluids*, 2015, **96**, 298.
33 Y. Zhang and C. Erkey, *J. Supercrit. Fluids*, 2006, **38**, 252.
34 W. Yu, Y. P. Hsu and C. S. Tan, *Appl. Catal., B*, 2016, **196**, 185.
35 C. H. Yen, H. W. Lin and C. S. Tan, *Catal. Today*, 2011, **174**, 121.
36 C. H. Yen, H. W. Lin, T. D. Phan and C. S. Tan, *J. Nanosci. Nanotechnol.*, 2011, **11**, 2465.
37 R. W. Stevens Jr, S. S. C. Chuang and B. H. Davis, *Appl. Catal., A*, 2003, **252**, 57.
38 R. W. Stevens Jr, S. S. C. Chuang and B. H. Davis, *Thermochim. Acta*, 2003, **407**, 61.
39 W. Yu, Y. Tang, L. Mo, P. Chen, H. Lou and X. Zheng, *Catal. Commun.*, 2011, **13**, 35.
40 Y. Yang, C. Ochoa-Hernández, V. A. de la Peña O'Shea, P. Pizarro, J. M. Coronado and D. P. Serrano, *Appl. Catal., B*, 2014, **145**, 91.
41 J. Ruan, T. Kjellman, Y. Sakamoto and V. Alfredsson, *Langmuir*, 2012, **28**, 11567.
42 W. H. Teoh, R. Mammucari and N. R. Foster, *J. Organomet. Chem.*, 2013, **724**, 102.
43 J. M. Escola, J. Aguado, D. P. Serrano, A. García, A. Peral, L. Briones, R. Calvo and E. Fernandez, *Appl. Catal., B*, 2011, **106**, 405.
44 A. J. J. Koekkoek, J. A. R. van Veen, P. B. Gerrtisen, P. Giltay, P. C. M. M. Magusin and E. J. M. Hensen, *Microporous Mesoporous Mater.*, 2012, **151**, 34.
45 D. Xu, R. G. Carbonell, D. J. Kiserow and G. W. Roberts, *Ind. Eng. Chem. Res.*, 2005, **44**, 6164.